Role of point-defect sinks on irradiation-induced compositional patterning in model binary alloys

Shipeng Shu, P. Bellon, and R. S. Averback

Role of point defect sinks on irradiation induced compositional patterning in model binary alloys

Shipeng Shu, P. Bellon and R.S. Averback

Department of Materials Science and Engineering, University of Illinois at Urbana-Champaign, Urbana, IL 61801, USA

Abstract:

The dynamical competition between the chemical mixing forced during energetic particle irradiation and thermally activated decomposition can lead to the stabilization of self-organized steady states in alloy systems comprised of immiscible elements. Continuum modeling and atomistic simulations predicted the stabilization of steady-state nanoscale compositional patterns for a well-defined range of ballistic mixing frequencies normalized by the irradiation-enhanced thermal atomic jump frequencies. Irradiation-induced compositional patterning has now indeed been observed experimentally, but a quantitative comparison has been lacking because models and simulations have relied on a simplified treatment with a fixed point defect concentration. We overcome here this limitation by using a kinetic Monte Carlo (KMC) code that includes the production, recombination, and elimination of point defects at sinks, as well as the chemical mixing forced by ballistic replacements. By varying the sink density and their efficiency, the temperature range of stabilization of steady-state compositional patterns is investigated in model binary alloys for point defect regimes dominated by either recombination or elimination on sinks. We find that in the sink regime, compositional patterning can be extended to remarkably high temperatures. The results are discussed by analyzing the relative diffusivities of A and B species, and their dependencies on temperature.

I.   Introduction

Materials subjected to continuous irradiation by energetic particles constitute

dynamical systems, whereby the disorder introduced by irradiation, in the form of non-

equilibrium point defects and forced chemical mixing, competes with thermally activated

relaxation toward equilibrium. This dynamical competition can trigger self-organization

reactions, such as the formation of voids and bubble lattices in pure metals [1,2], and the

stabilization of nanoscale compositional patterns in multi-phase alloys [3,4]. The latter

reaction, which is the focus of this work, has been studied and rationalized using

atomistic simulations [5,6] and continuum modeling [7]. The dynamical stabilization of

nanoscale composition patterns results in microstructures with a high density of chemical

interfaces under irradiation. These interfaces are of interest since they are potential traps

for point defects. They are therefore likely to limit long range diffusion, and with it,

degradation of the material from swelling, irradiation creep, or radiation-induced

segregation and precipitation [2,8-14]. Implementation of this approach requires the

ability to control and tune the regime where compositional patterns are stable under

irradiation. In particular, as many advanced nuclear reactor designs call for very high

temperatures of operation [9,15], a significant challenge is to extend the patterning

regime to these high temperatures. We demonstrate in the present work that the

introduction of a high number density of point defect sinks can dramatically extend the

stability of the patterning regime.

The influence of sinks on irradiation-induced composition patterning can be

readily seen using as an example the model proposed by Enrique and Bellon [5,7]. This

model employs a phase-field-type approach to calculate dynamical phase diagrams,

representing the most stable steady state under given irradiation conditions. For an equiatomic *A-B* model alloy, comprised of immiscible elements, two parameters control the evolution and stability of the composition field. The first parameter γ characterizes the forcing intensity, while the second parameter, *R,* refers to the characteristic relocation distance of atomic mixing events. The forcing intensity is defined as the ratio,

$$\gamma = \frac{\Gamma}{\tilde{D}_{irr}} \qquad\qquad (1)$$

where $\tilde{D}_{irr}$ is the chemical diffusion coefficient, typically accelerated by the supersaturation of irradiation-induced point defects, and Γ is the ballistic jump frequency. Γ is directly related to the atomic displacement rate, K_0, through $\Gamma = bK_0$, where *b* is the number of atoms undergoing ballistic relocation per atomic displacement [16][17]. At temperatures below the equilibrium critical temperature of the binary alloy T_c, three possible steady states were identified in the (γ, R) parameter space, as illustrated in Figure 1. At large γ, ballistic mixing dominates and forces the system into a solid solution, while at low γ and R values, thermally activated diffusion wins out and maintains macroscopic phase separation. At intermediate γ values, and with *R* exceeding a critical value R_c, a third steady state evolves, where compositional patterns with a finite length scale are stabilized. These types of patterns have indeed been observed experimentally, initially by Nelson et al. in order-disorder alloys [3], and more recently by Krasnochtchekov et al. [18], Chee et al. [4] and Stumphy et al. [19,20] in Cu-base immiscible alloy systems. These experiments also support the model prediction that the transition from the compositional patterning to macroscopic phase separation, the γ_1

boundary in Figure 1, should be a first-order type transition, with a discontinuity of the characteristic phase separation length scale, from nanometric in the patterning regime to macroscopic in the coarsening regime.
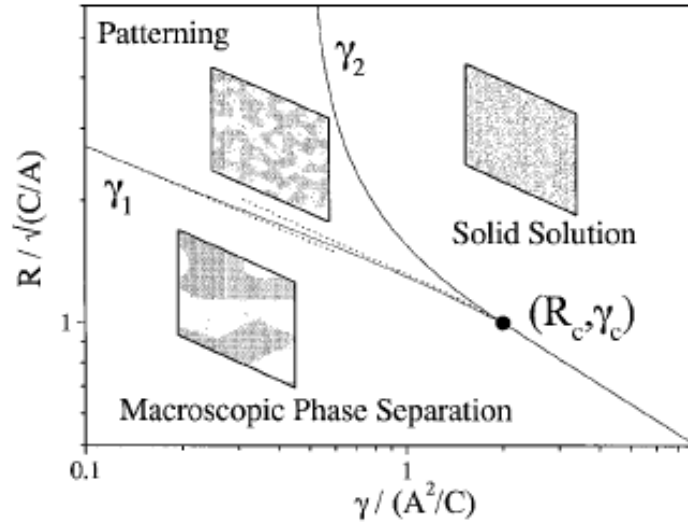
Figure 1. Steady-state phase diagram for an equiatomic model immiscible binary alloy. R is the average relocation distance of ballistic jumps, and γ represents the forcing intensity (see text and Eq. (1) for definition). R and γ are given in units of the A and C Ginzburg-Landau free energy parameters used in ref. [7]. Adapted from ref. [7].

The dependence of γ with temperature, and thus the temperature range of the compositional patterning regime, is dictated by the chemical diffusion coefficient, as ballistic mixing is largely independent of temperature. It is well recognized that the dependence of the radiation-enhanced diffusion coefficient on temperature and displacement rate is a function of the alloy microstructure. This dependence can be estimated, for instance, using standard rate theory [21], as illustrated next. For the simple case of infinitely dilute alloys, the chemical diffusion coefficient entering in the denominator of Eq. (1) can be approximated by the radiation-enhanced solute (*B* atom)

diffusion coefficient in an A-atom matrix, D_B^{irr}. At low temperatures and sink densities,

recombination is the dominant mechanism of point defect annihilation, and D_B^{irr} is

proportional to $\Gamma^{1/2} D_V^{1/2}$ [16,21], where D_V is the vacancy diffusivity. In this

recombination regime, therefore, the forcing intensity scales as $\gamma \propto \Gamma^{1/2} D_V^{-1/2}$, and it thus

decreases continuously as the irradiation temperature increases. Eventually, γ will cross

the γ_1 boundary and the system will undergo macroscopic precipitate growth. If the alloy

microstructure possesses a sufficiently high density of effective sinks, on the other hand,

vacancies and interstitials will be lost predominantly at sinks. Accordingly, the solute

diffusion coefficient scales as $D_B^{irr} \propto \Gamma(D_V)^0$, and therefore the forcing intensity is

independent of both Γ and T. Therefore, if the alloy microstructure can be tailored to

contain a high density of stable sinks, compositional patterning could be stable at high

temperatures, as the forcing intensity would never cross the γ_1 boundary. This prediction

is however quite speculative since diffusion in alloys under irradiation is far more

complex than assumed in the above discussion, owing to the coupling between chemical

and defect fluxes [22]. Moreover the sink efficiency of irradiated microstructures is likely

to evolve, albeit slowly, as precipitate and dislocation densities are affected by the

irradiation temperature and the displacement rate. In the present work, we overcome

many of these complexities encountered by rate theory in studying compositional

patterning by using kinetic Monte Carlo (KMC) simulations. We note that the KMC

model developed here includes both the effects of radiation-induced ballistic mixing,

which plays an essential role in stabilizing compositional patterns, and the *non-conserved*

character of point defects, which can lead to the redistribution of chemical species under

irradiation. As detailed below, this extended model now makes it possible to investigate the influences of point defect sinks and radiation-induced fluxes on compositional patterning.

II. Method

1. Kinetic model and KMC simulations

The kinetic model employed in the present simulations is a combination of the models developed by Enrique and Bellon [5], to study compositional patterning under irradiation, and Soisson [23], to study the effects of sinks on radiation induced segregation. In particular, the model includes finite-range ballistic mixing, defect production, and defect annihilation. The main ingredients of the model are summarized as follows (details of the model are given in Appendix A). Atoms are assumed to migrate either by thermally activated jumps, mediated by vacancies and interstitials, or by athermal, ballistic relocations forced by irradiation. Atoms are located on a perfect, rigid, face-centered cubic (fcc) lattice, having periodic boundary conditions. The resulting simulation volume is a $L_1 a_{nn} \times L_2 a_{nn} \times L_3 a_{nn}$ rhombohedron whose faces are {111} planes of the fcc lattice, $a_{nn} = \sqrt{2}a / 2$ being the nearest neighbor distance of the fcc lattice of lattice parameter a. Irradiation induced Frenkel pairs, i.e., vacancies (V) and dumbbell interstitials (I), are introduced randomly into the system at a rate specified in units of displacements per atom (dpa) per second. The model for defect generation, migration, and annihilation on sinks is similar to the one described by Soisson [23], for a bcc lattice. For simplicity, we ignore point defect clustering, during both defect production and migration. The impact of this approximation will be discussed in Section IV.

The internal energy of a given atomic configuration is computed as the sum of nearest neighbor pair interactions, including atom-atom interactions ($\varepsilon_{AA}, \varepsilon_{AB}, \varepsilon_{BB}$) and effective atom-vacancies and atom-interstitial dumbbell interactions ($\varepsilon_{AV}, \varepsilon_{BV}, \varepsilon_{AI}, \varepsilon_{BI}$, I = AA, AB, BB). These interaction energies determine the cohesive energy of the pure elements, the mixing enthalpy of the alloys, and the defect formation energies. Values of ε_{ij} were selected to give an ordering energy of $\omega_{AB} = 0.0553 eV$, yielding a critical temperature for phase separation of $T_c = 1573K$. The frequency of all thermal jumps is determined using standard rate theory, with the activation energy calculated by a broken-bond model,

$$\Delta E_{XV} = E_{XV}^{SP} - \sum_m \varepsilon_{mX} - \sum_n \varepsilon_{nV} \qquad (1)$$

$$\Delta E_{XI} = E_{XI}^{SP} - \sum_m \varepsilon_{mX} - \sum_n \varepsilon_{nI} \qquad (2)$$

where m and n label the nearest-neighbor sites of point defect (V or I) and atom X, respectively. The saddle point energies E_{XV}^{SP} and E_{XI}^{SP} are the interaction energies between the atom-defect complex and the surrounding atoms at the saddle point configuration. With a predetermined set of pair interactions, the saddle point energy is set by the activation energy for the migration of the corresponding defect. We assume here for simplicity that these saddle point energies depend on the identity of the jumping atoms, but not on their environment. The parametrization of these saddle point energies is detailed later in this section.

Once created, the point defects migrate on the lattice through thermally activated jumps until they either recombine or reach a sink. Sinks are defined as sets of lattice sites where the point defects have a pre-defined, non-zero probability p to be absorbed. Perfect sinks are characterized by $p=1$. The ballistic mixing forced by nuclear collisions is modeled by randomly exchanging atoms at a certain frequency, which is calculated by multiplying the displacement rate, K_0 by b, the number of relocations per displacement. Following Enrique et al. [6], the distribution of relocation distances is chosen to be an exponential-decay, $\exp(-r/R)$, where r is the relocation distance, and the average relocation distance, R is set to be $R=1.5a_{nn}$. This value is a little larger than the average relocation distance determined by molecular dynamics (MD) simulations for Cu-Ag alloys, 1.09 a_{nn}. We have used this somewhat larger average relocation distance since it increases the region of compositional patterning (see Figure 1), and enhances the effects illustrated in the present parametric study.

The kinetic evolution of the system is constructed using the residence-time algorithm [24], considering all possible events at each KMC step. After each time step, the algorithm checks whether recombination or absorption at sinks should take place based on the rules given previously. When recombination or defect elimination at sinks occurs, the KMC time is not changed, since we consider these events to be instantaneous.

The particular thermo-kinetic parameters used in the KMC simulations are listed in Appendix A, Table 1. As indicated in Section I, the present modeling work is motivated in part by experimental work on dilute Cu-base alloys. The parameters of the A metal have thus been chosen to be representative of Cu. We note that Cu has a fairly

small atomic volume, and thus for many copper alloys, such as Cu-Ag and Cu-Nb, the

solute species is oversized compared to Cu atom, making mixed dumbbells and solute

dumbbells unstable in the Cu matrix. We thus set the formation energies of *AB* and *BB*

dumbbells in *A* significantly larger than the other formation energies, see Appendix A

Table 1 for details. Turning next to vacancy-mediated transport, the relative diffusivity of

the solute and solvent species can be different from alloy to alloy. For example, in a Cu

matrix, the thermal diffusivity of Ag atom is larger than that of Cu; that for Fe is similar;

while the diffusivity of Co is smaller [25-27]. In the present work, we thus employ three

different parameter sets, so as to investigate the effect of the relative diffusivity of solute

and solvent atoms. These three parameter sets are obtained by varying the saddle point

energy for the *B*-vacancy exchange in pure *A*, see Table 1 in Appendix A. The saddle

point energy for the *A*-vacancy exchange in pure *A* is kept constant, and its value is

chosen so that the vacancy migration energy in pure *A* is 0.8 eV, close to the

experimental value for Cu [28]. As seen in Figure 2, in the dilute limit, the ratio of partial

diffusivities by vacancy motion, d_B^V / d_A^V, is less than one, equal to one, and greater than

one for the parameter set 1, 2, and 3, respectively. Note also that the ratios of partial

diffusivities depend differently on temperature, either increasing, constant, or decreasing

with temperature for parameter set 1, 2, and 3, respectively.
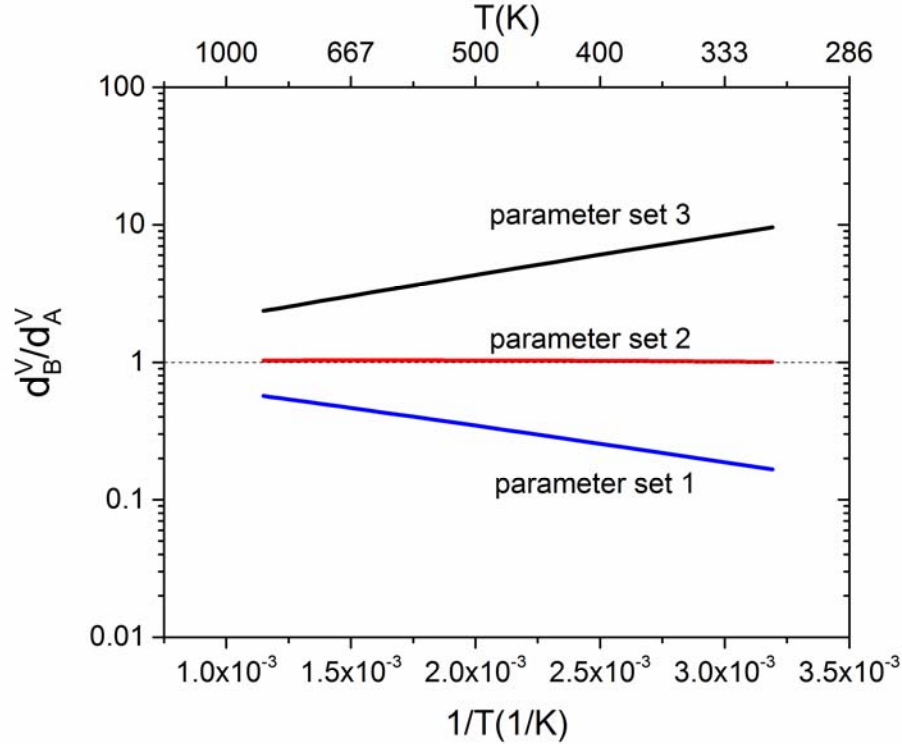
Figure 2. Ratio of partial diffusion coefficients of *A* and *B* atoms via vacancy diffusion mechanism, as a function of temperature, for the three alloy parameter sets (see Table 1 for definitions). (Color online)

Two sink geometries are considered in this work, planar and spherical. The first situation corresponds to multilayer composites, while the second situation represents semi-coherent or incoherent precipitates. Simulations are run until the system reaches steady state, as monitored by the structure factor. Typically, for systems with spherical sinks, each run is comprised of 800 iterations of 1×10^9 jumps, which corresponds to 3×10^6 jumps per atom. For selected simulations, we verified that the system reaches a unique steady state by using two very different initial configurations, a random solution and a single *B* precipitate embedded in the *A* matrix.

We first use the simulation to consider a pure metal, using both planar and spherical sinks. This is done to validate the KMC model by comparing the computed

defect concentration profiles with analytic results from rate theory. We then examine

compositional patterning in alloys using spherical sinks. In this case, we use the structure

factor $S(\mathbf{k})$, which is the Fourier transform of the pair correlation function, to distinguish

the three possible steady states illustrated in Figure 1 [29]. The simulated microstructures

are on average isotropic, and it is thus sufficient to consider the spherically averaged

structure factor $S(k)$:

$$S(k) = \frac{1}{4\pi} \int S(\mathbf{k}) \, \mathrm{d}\Omega \qquad (3)$$

In the case of a solid solution, $S(k)$ decreases monotonously with k, following closely a

Lorentzian shape. In the patterning regime, the maximum of $S(k)$ is located at a finite k

value, and the intensity of that peak is independent of the size of the system [29,30]. In

order to obtain a characteristic decomposition length scale, we calculate the first moment

of $S(k)$. In the macroscopic phase separated regime, $S(k)$ is maximum for the first nonzero

k point, i.e., the system decomposes at the largest length scale compatible with the

simulation cell size.

2. Point defect evolutions from rate theory

We briefly recall here some key results obtained from rate theory on point defect

evolutions in pure metals under irradiation [23]. We use these expressions in Section III

to validate our KMC simulations and to introduce a criterion for the transition between

defect elimination regimes. In the absence of defect clustering, the evolution of point

defect concentrations can be described by two reaction-diffusion equations [21]

$$\frac{\partial c_v}{\partial t} = K_0 - K_{iv}c_ic_v - K_{sv}c_sc_v + D_v\nabla^2 c_v$$

$$\frac{\partial c_i}{\partial t} = K_0 - K_{iv}c_ic_v - K_{si}c_sc_i + D_i\nabla^2 c_i$$

(4)

where K_0 is the defect production rate of Frenkel pairs, K_{iv}, K_{sv}, K_{si} are rate constants

for recombination and defect-sink reactions, the subscripts v, i, and s, referring to

vacancies, interstitials, and sinks. We focus here on steady states, i.e.,

$\partial c_v / \partial t = \partial c_i / \partial t = 0$, and consider two simple situations: planar sinks and spherical sinks.

We first consider in Section III the case of planar sinks, which is relevant for

multilayered samples. Demkowicz and coworkers have used this geometry to evaluate the

effect of imperfect sinks on both the average defect concentration and the concentration

profile [31]. In this case, there are no distributed sinks, and thus the K_{sv} and K_{si} terms

are set to zero and the boundary conditions become

$$c_v\big|_{x=0,l} = c_v^e, \quad c_i\big|_{x=0,l} = c_i^e,$$

(5)

where c_v^e and c_i^e are the equilibrium vacancy and interstitial concentration. For an imperfect

sink, the sink efficiency η is defined as [32]

$$\eta = \frac{J_{imperfect}}{J_{perfect}},$$

(6)

where $J_{imperfect}$ and $J_{perfect}$ are the defect flux into the interface for an imperfect and a

perfect sink, respectively. Solving the simplified governing equations numerically with

this new imposed boundary conditions, Demkowicz *et al.* [31] obtained the average

defect concentrations within the entire cell and concentration profiles along the domain.

III. Results

III.1. Defect regimes in irradiated pure metal

We first reconsider the case of a layered structure to test our KMC model. We thus introduce a planar sink on one of the {111} planes terminating the rhombohedral simulation cell; owing to the periodic boundary conditions, this represents a layered geometry. The results presented below are for a system size of $200 \times 200 \times 96$; additional results with different system sizes are given in Appendix B. At $T = 406$ K, which corresponds to $\sim 0.25 \, T_c$, a series of simulations was carried out with different absorption probabilities p, simulating sinks of different efficiencies. The defect production rate was set to $5 \times 10^{-4} \, dpa / s$. The resulting steady state vacancy concentration profiles are compared in Figure 3 with the solutions to the reaction-diffusion Eq. (4). Note that in the calculated profiles the sink efficiency η is not fitted, but it is instead obtained directly from the KMC simulations using Eq. (6) and then used as the flux boundary condition for solving Eq. (4). The profiles illustrate the expected result that less efficient sinks lead to higher vacancy concentrations. The flat portion of the profiles away from the sinks corresponds to a region where the dominant mechanism for defect elimination is recombination.
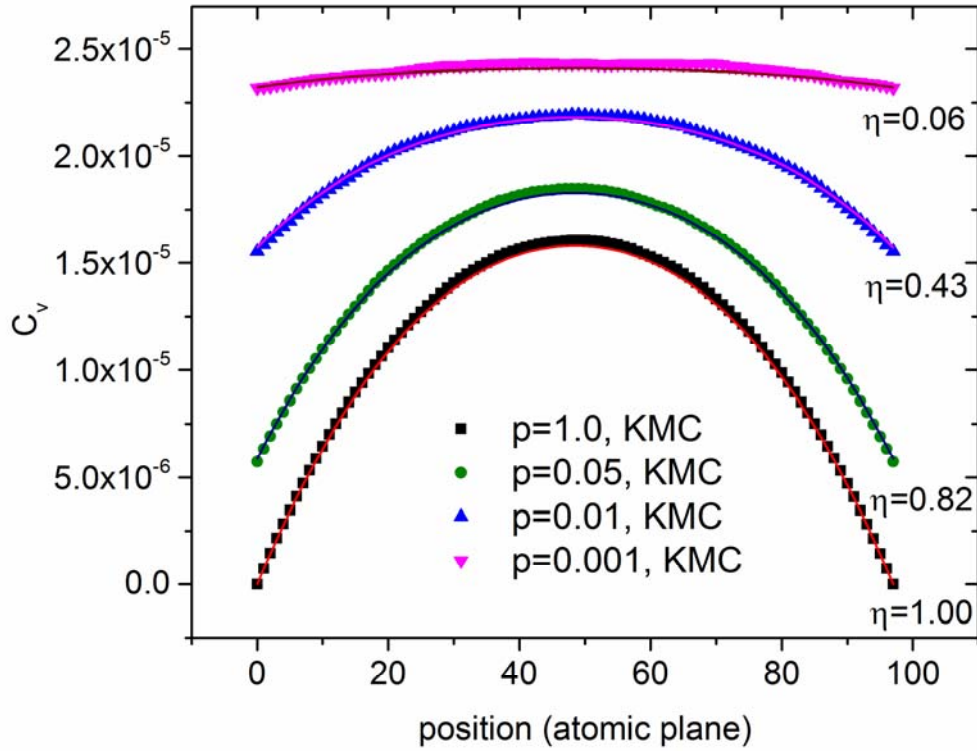
Figure 3. Vacancy concentration profile for a planar sink geometry as a function of sink absorption probability, *p*. η is the sink efficiency measured in the KMC simulation and used as input for rate theory calculation. Symbols are the KMC simulation results; solid lines are the results of rate theory (Color online)

The results shown in Figure 3, along with others using different layer thicknesses (see Appendix B) clearly illustrate that the steady-state vacancy concentration, and thus the sink efficiency as defined by Eq. (6), is a function of both the sink absorption probability *p* and the distance between sinks. As expected, the sink efficiency η indeed varies with the layer thickness for a given absorption probability *p*. The sink efficiency η defined by Eq. (6), therefore, is not an intrinsic property of a sink, like *p*, as its value depends on the layer thickness [31].

We next consider whether defects annihilate primarily by recombination or at sinks, as this will help in understanding the compositional patterning behavior, namely, its dependence on temperature and irradiation flux. The criterion that is often used in rate theory to make this determination is based on the dependence of atomic diffusion coefficients with temperature or displacement rate [21]. We suggest here a simpler approach, one that considers only the fraction of point defects eliminated by recombination; this quantity is readily available in KMC.

A set of simulations was thus carried out at various temperatures, keeping the displacement rate constant, to determine atomic diffusion coefficients and the fractions of vacancies annihilated by recombination with interstitials. The atomic diffusion coefficient was obtained as the product of the steady-state vacancy concentration measured in the KMC simulations and the vacancy diffusion coefficient [21], the latter being directly calculated using the parameters given in Table 1. In this calculation, and in the following ones, we ignore the effect of correlation factors on vacancy and atomic diffusion since they do not vary significantly in the temperature range examined. At low temperatures, the A diffusion coefficient increases as temperature increases, see Figure 4 (a) and (b), with an apparent activation energy of 0.4 eV, equaling half of the vacancy migration energy, in agreement with rate theory for the recombination regime. At higher temperatures, the increase of the atomic diffusion coefficient plateaus, which in rate theory corresponds to the sink elimination regime. As expected in this regime, the plateau value scales linearly with the displacement rate (results not shown here). The transition temperature between the two defect regimes was taken as the point where the two asymptotic behaviors intersect, as illustrated in Figure 4. The KMC measured

recombination fractions at this crossover are 28.3% and 32.1% for perfect sinks ($p = 1$)

and imperfect sinks ($p = 10^{-3}$), respectively. One can also estimate the intersection of

these asymptotic regimes by using the steady-state solutions of Eq. (4) for uniform defect

concentrations, i.e., without the Laplacian terms, to calculate the diffusion coefficients

under irradiation. This procedure yields a cross-over recombination fraction of

$\left(\sqrt{5} - 1\right)/4 \approx 0.309$, thus in very good agreement with the KMC results. The rate theory

calculation suggests that the recombination fraction at the cross-over should be

independent of the sink geometry. Results obtained for the case of spherical sinks,

detailed in Appendix C, yield a recombination fraction of $\approx 29\%$, thus supporting the

above analysis. In Section III.2, we will thus use a recombination fraction of 30% as the

boundary separating the recombination and sink-limited regimes.

(a)

(b)
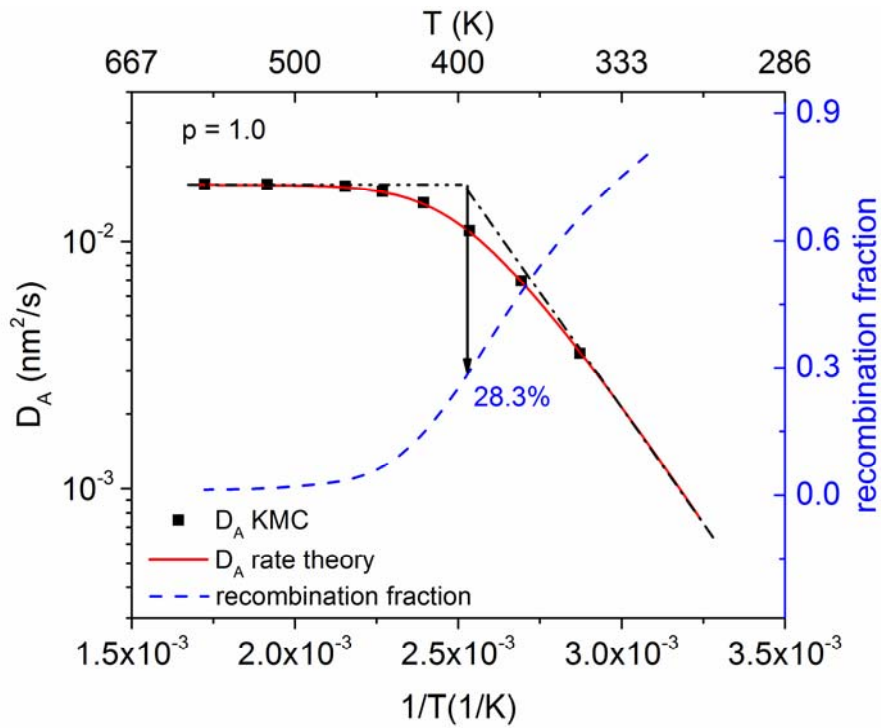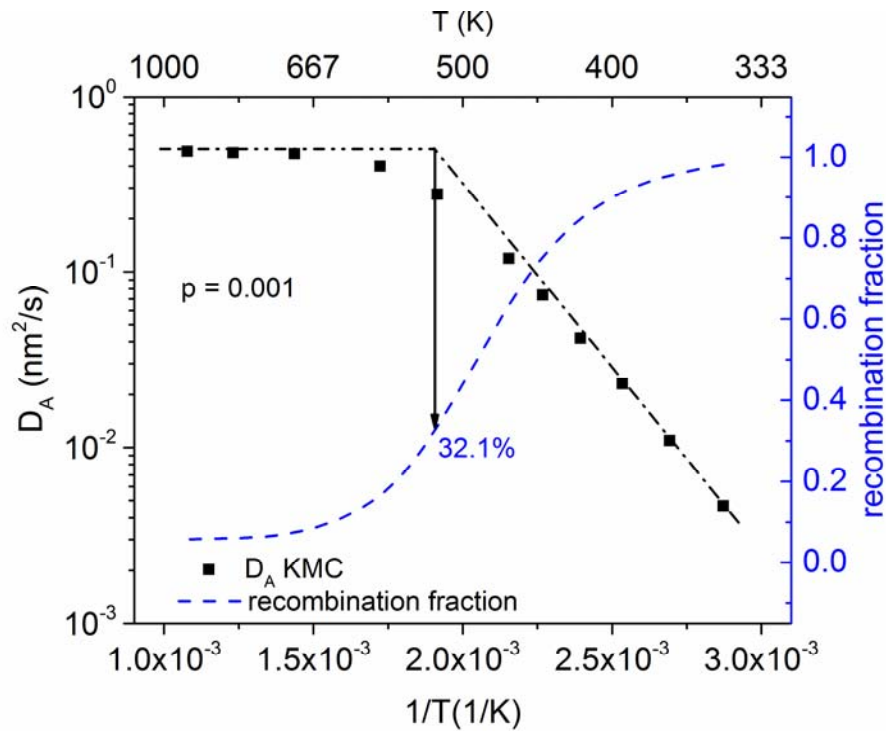
Figure 4. *A* atomic diffusion coefficient and the KMC measured recombination fraction as a function of temperature for planar sink geometry. (a) perfect sinks, $p = 1.0$ (b) imperfect sinks, $p = 0.001$. The dash-dot lines are the asymptotic lines of the

recombination and sink elimination regimes; their intersection corresponds to the transition point. (Color online)

III.2.   Effect of sinks on compositional patterning in irradiated alloys

We next examine the effect of sinks on compositional patterning in immiscible alloys. The solute concentration selected for this study is 12 at.% *B*, as it is high enough compared to the solute solubility under irradiation to result in the formation of precipitates that are easy to identify and characterize, but low enough to prevent the formation of connected precipitates. We begin with patterning in the recombination regime, and then turn to the sink elimination regime.

III.2.1. Patterning in the recombination regime
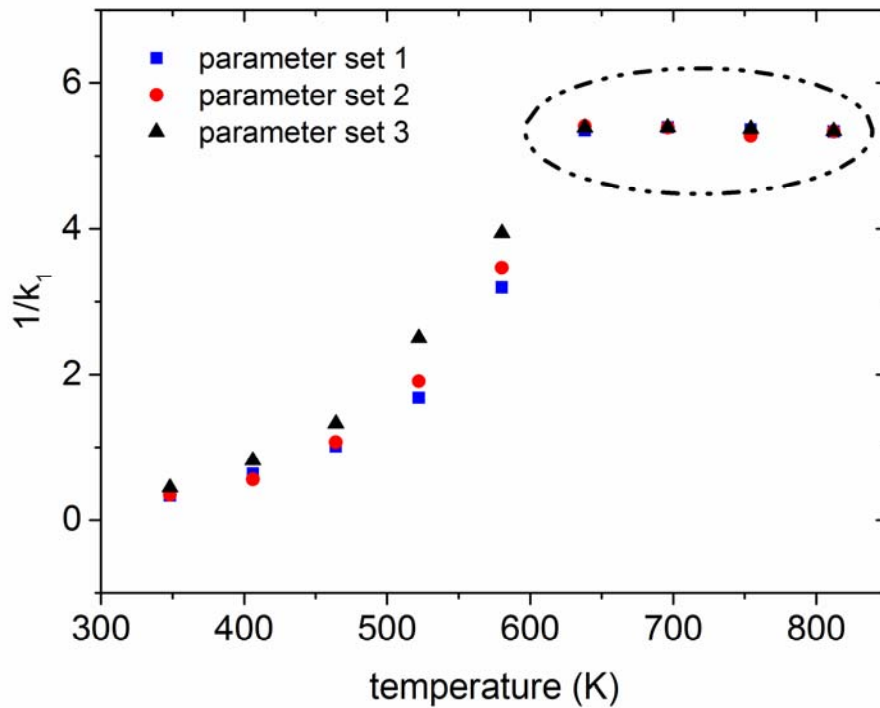
Figure 5. Steady state phase separation length scale as a function of temperature for three parameter sets for the low sink strength case. The length scale is given by the inverse of

the first moment of structure factor, in unit of a. The largest possible phase separation length scale compatible with the 64^3 simulation cell equals to $64a/(2\pi\sqrt{3}) \approx 5.88a$. In the figure, for points at high temperatures, the length scale of the circled data points is limited by the size of simulation cell, and would be larger with a larger simulation cell. (Color online)

In this section, we consider a 64^3 alloy with one spherical sink. This yields a relatively low sink density, $3.2 \times 10^{23} m^{-3}$. We also choose a low absorption probability p = 0.001 so that recombination is the dominant mechanism for point defect annihilation. Specifically, the recombination fraction will be greater than 90% for all parameters used in this sub-section. As irradiation temperature is increased while keeping the displacement and the ballistic mixing rates constant, the solute diffusion coefficient increases, and accordingly the value of the forcing parameter γ decreases. We expect, therefore, that as the temperature increases the steady-state microstructure will first undergo a transition from solid solution to compositional patterning, and then from compositional patterning to macroscopic phase separation. In order to study the effect of alloy properties on compositional patterning, three different sets of parameters are used, leading to three different relative diffusivities between solute and solvent atoms. For parameter sets 1, 2, and 3, the partial diffusion coefficient of B by vacancy diffusion is smaller, equal to, and larger than that of A, respectively. The number of ballistic relocations per displacement, b is fixed at 20 for each case, a value typical of light to medium mass ion irradiations [33], and the displacement rate is set to 5×10^{-4} dpa/s. The evolution of the steady-state decomposition length scale is plotted in Figure 5 as a function of the irradiation temperature. For all three sets of parameters, the steady-state structure factors shows that the systems undergo a transition from the compositional

patterning regime to the macroscopic phase separation regime as temperature increases.

The transition temperatures are similar for the three parameter sets, as they all lie

between 580 K and 638 K. Figure 6 shows the steady state structure factors and

microstructures for parameter set 3 near the transition. At 522 K, the structure factor has

a peak at finite wave vector, characteristic of the compositional patterning regime. At 580

K the structure factor has a maximum at the first k point, however, its intensity is low

compared to that of a macroscopically phase separated system and it does not increase

with time. This suggests that the system still lies within the patterning regime. In contrast,

the structure factor is very large on the first k point at 638 K, suggesting macroscopic

phase separation. Direct visualization of steady-state microstructures provides further

support for these conclusions. In particular, at 638 K, the microstructure contains only

one precipitate, see Figure 6 (d), and it is thus decomposed at the largest scale allowed by

the size of the simulation cell; in contrast, at 522 K and 580 K, multiple finite size

precipitates are observed in (b) and (c). Noteworthy in these figures are small A

precipitates inside B precipitates. Such microstructures, referred to "cherry-pit" structures,

were reported previously both in experiments [19,20] and in KMC simulations [34]. This

structure will not be discussed here in further detail, but the interested reader is referred

to the above references.
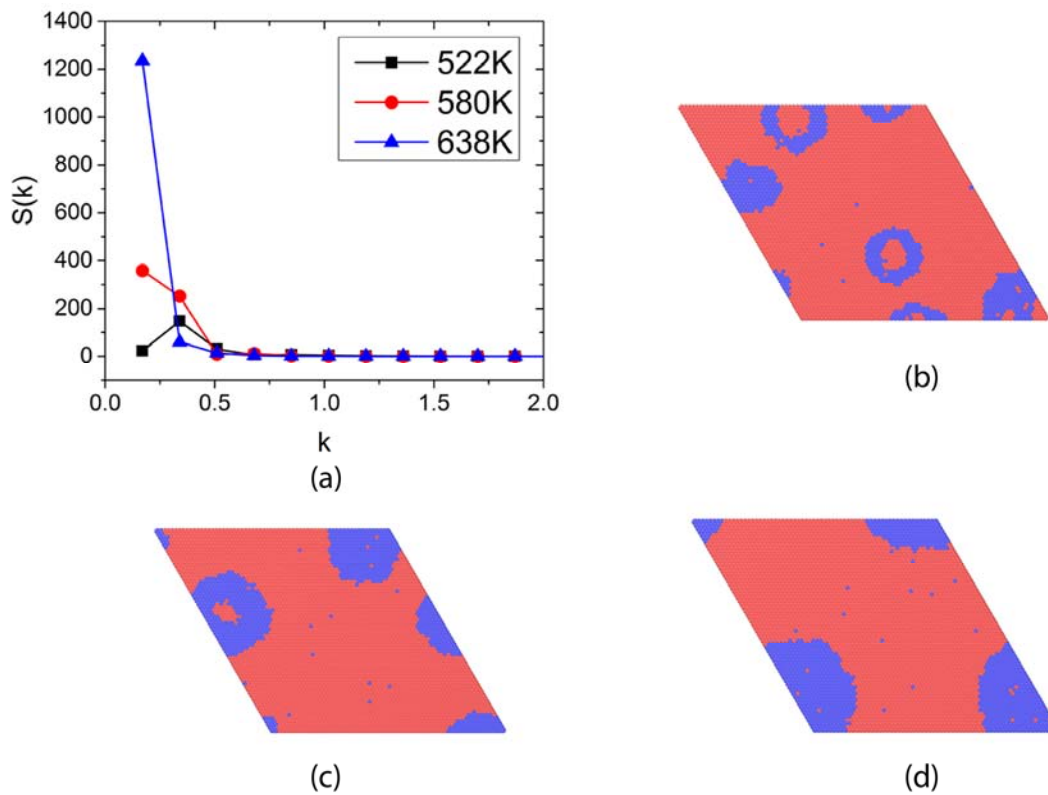
Figure 6. (a) structure factor evolution near the transition temperature for parameter set 3, $b = 20$. The wave vector k is given in unit of $1 / a$. (b) microstructure at 522 K (b) microstructure at 580 K (b) microstructure at 638 K. Red: A, blue: B. (Color online)

III.2.2.　　　　Patterning in the sink elimination regime
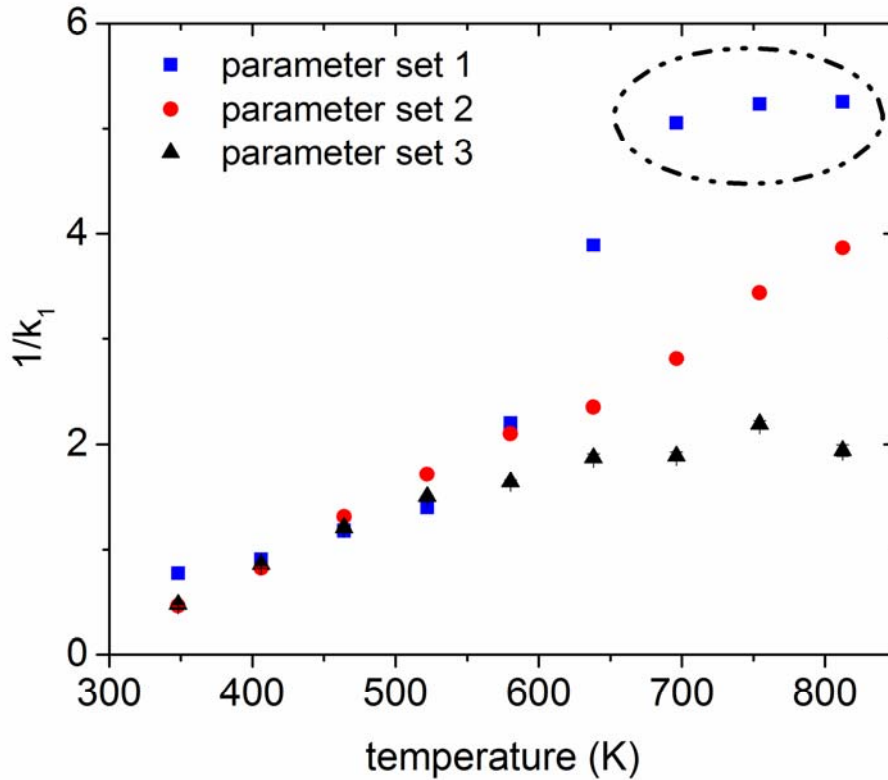
Figure 7. Phase separation length scale as a function of temperature for three parameter sets for high sink strength case. $p = 1.0$, 8 perfect sinks in the simulation cell. The length scale is given by the inverse of the first moment of structure factor, in unit of a. The largest possible phase separation length scale compatible with the 64^3 simulation cell equals to $64a/(2\pi\sqrt{3}) \approx 5.88a$. In the figure, for points at high temperatures, the length scale of the circled data points is limited by the size of simulation cell. (Color online)

Patterning in the sink l imited regime is quite different. This regime is of potential applied interest as it can extend the temperature range of patterning, as discussed in the Introduction. In order to favor annihilation of point defects at sinks, we increase the sink density by a factor 8, to $2.6 \times 10^{24} m^{-3}$, and employ perfect sinks, i.e., $p = 1$. The high sink density and efficiency result in the sink elimination regime being dominant for irradiation temperatures above ≈ 400 K. The number of ballistic relocations per displacement, b is set to be *20, 40* and *175* for parameter set 1 to 3. This setting leads to similar phase

separation length scale at lower temperatures for the three cases, and allows us to examine the patterning evolution for all three cases at the same temperature range.

In Figure 7, the phase separation length scale is plotted as a function of temperature. The precipitate evolutions are seen to be distinctively different for the three alloys, and in some cases they depart from the simple predictions obtained using rate theory for estimating the forcing parameter γ. For parameter set 3, i.e., $d_B^V / d_A^V > 1$, the evolution is close to that predicted by this simple approach, as patterning is extended to high irradiation temperatures and the decomposition length scale (or precipitate size) is nearly independent of the irradiation temperature in the range 500 K − 800 K. The slight decrease of the precipitate size at 800 K is due to an increase in solute solubility at this high temperature. For parameter set 2, $d_B^V / d_A^V = 1$, the system also remains in the patterning regime, however, the steady-state size increases continuously with temperature. For parameter set 1, the phase separation length scale increases with temperature, with the system undergoing a transition from patterning to "large-scale" phase separation at ≈ 700 K, as described below.

Direct visualization of the steady state configurations reveals important additional differences between the three alloys. Figure 8 shows that at 580 K B-rich precipitates form predominantly around the sinks for parameter set 1, but away from the sinks for parameter sets 2 and 3. The different morphologies will be rationalized in the Discussion section based on the coupling between solute fluxes and defect fluxes. We note that, cherry-pit precipitate structures are also observed in this regime (Figure 6), especially in the larger precipitates. Lastly, the microstructures for parameter set 1, see Figure 8 (a-d), suggest a transition to a large-scale phase separation regime between 580 K and 696 K.

The characteristic length-scale of this phase separation could be either the size of the system, as in the macroscopic phase separation identified in the recombination regime in section III.2.1, or it could be determined by the separation distance between sinks. A definitive answer to this question, however, would require much larger simulation volumes so as to vary separately the simulation cell size and the sink separation distance. These simulations are beyond our present capabilities and therefore we defer additional discussion of this point to a later time.
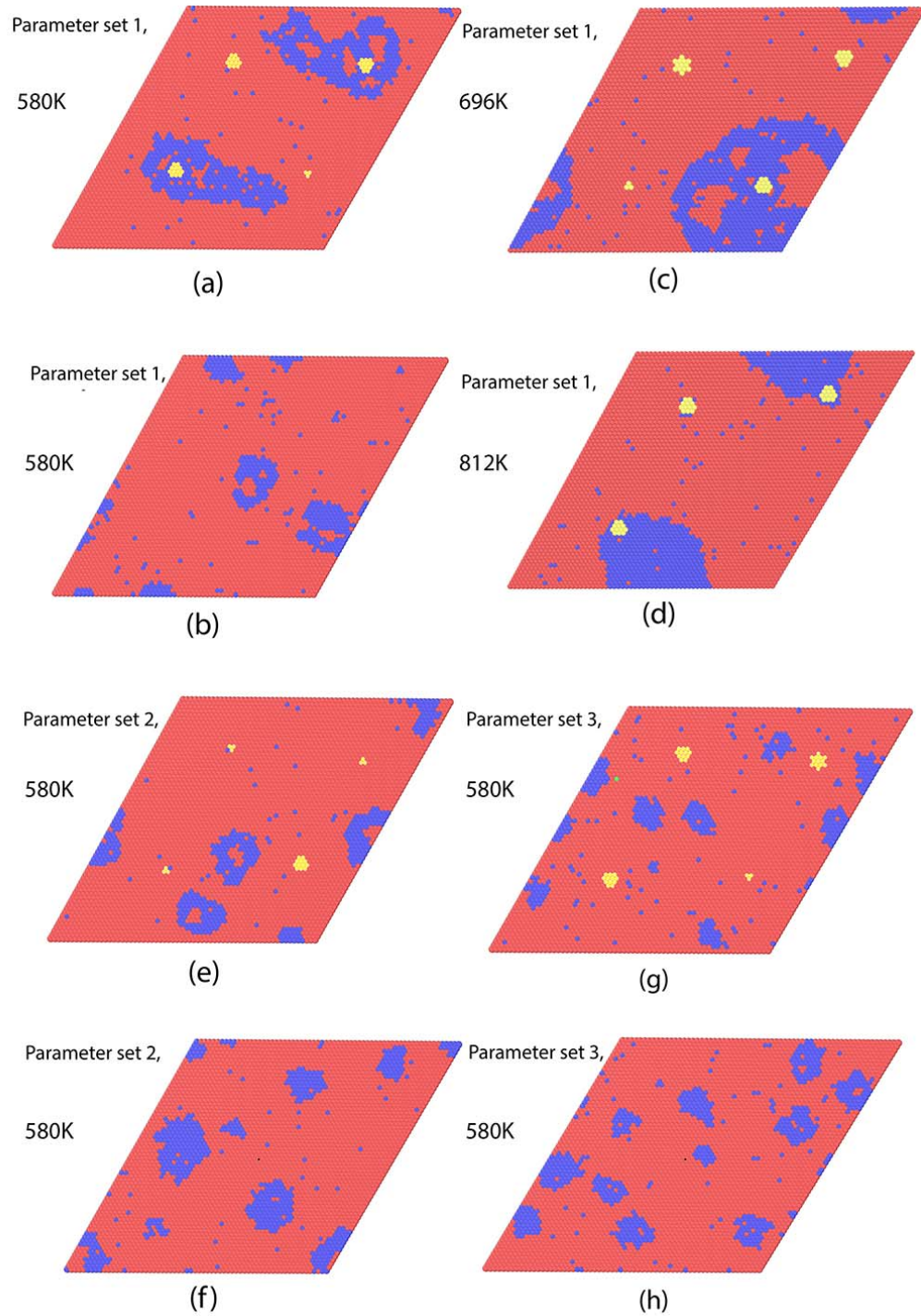
Figure 8. Steady state microstructures in (111) planes containing sinks or half-way between sinks for three parameter sets: (a) and (b) parameter set 1 at 580 K, (c) parameter set 1 at 696 K, (d) parameter set 1 at 812 K, (e) and (f) parameter set 2 at 580 K, (g) and (h) parameter set 3 at 580 K. (a), (c), (d), (e) and (g) are (111) cuts in a plane containing

the sinks; (b), (f) and (h) are (111) cuts half-way between the sinks. Red: *A* atoms, blue: *B* atoms, yellow: sink sites (Color online).

IV. Discussion

The main objective of this work has been to investigate the effect of the non-conservative character of point defects on irradiation-induced compositional patterning, and in particular on the range of irradiation temperatures over which patterning can be observed. We investigated the possibility of an extended stability of compositional patterning in the sink-dominated regime using atomistic simulations, so as to describe on the same footing chemical and point defect evolutions. More specifically, we employed kinetic Monte Carlo simulations relying on a kinetic model that combines finite range chemical mixing as modeled by Enrique et al. [5,6], with the creation, recombination and sink elimination of point defects, following the procedure proposed by Soisson [23]. This model was first validated by considering the case of a pure metal, by comparing diffusion coefficients to the values predicted from rate theory for systems with planar or spherical sinks. The agreement between the two approaches is very good, and the transition from the sink-dominated regime at high temperature to the recombination-dominated regime at low temperature takes place when the recombination fraction reaches ≈ 30 %, in agreement with rate theory.

The KMC simulations were applied to several model immiscible binary alloys, using irradiation parameters that allowed stabilization of compositional patterning at steady state [5,7]. The domain of stability of compositional patterning was investigated as a function of irradiation temperature with sink density and efficiency such that the point

defect evolution is controlled either by recombination or by elimination on sinks. In the recombination regime, the three alloys considered for the present KMC simulations showed a transition from compositional patterning at lower temperature to macroscopic phase separation at higher temperature. This transition is expected within the Enrique-Bellon model since, in the recombination regime, the forcing intensity should scale as $\gamma \propto K_0^{1/2} D_V^{-1/2}$, and therefore increasing the irradiation temperature should lead to a continuous decrease of γ. Eventually the system crosses the γ_1 boundary in Figure 1. The transition temperatures from patterning to macroscopic phase separation are similar for the three alloys, at least to within the 60 K temperature steps used in this study. This small shift, if any, is consistent with a transition temperature shift of $\approx$ 30 K calculated from the change in diffusion coefficient values between the alloy parameter set 1 to set 3. One effect that is however not included in the Enrique-Bellon model is the composition dependence of the interdiffusion coefficient. The present study indicates that the larger the solute diffusion coefficient, as is the case with parameter set 3, the larger the steady state size of the precipitates. This is a first illustration of the important role played by alloying effects.

In the sink elimination regime, a more intriguing situation is expected since, using rate theory for calculating atomic diffusion as function of the irradiation parameters, the forcing parameter should now scale as $\gamma \propto (K_0)^0 (D_V)^0$. This scaling suggests that the forcing parameter should be independent of both the irradiation temperature and displacement rate, and result in an unlimited extension of the domain of stability of compositional patterning at higher temperatures, until equilibrium vacancies come into play.

The KMC simulations indeed indicate that in the sink-dominated regime, the phase separation length scale has a weak temperature dependence, especially for parameter sets 2 and 3, extending the compositional patterning regime to ~ 800 K. The maximum patterning temperature in the simulations is in fact limited by the increase in solute solubility at these high temperatures, which leads to a reduction in the precipitate volume fraction (for the parameters used in the simulations, thermal vacancies outnumber point defects created by irradiation at temperatures above ~700 K, but, for simplicity, they were not included). In the case of parameter set 1, a transition from compositional patterning to another decomposition regime, with a coarser characteristic length scale, took place between 638 K and 700 K, even though the point defect kinetics remained in the sink elimination regime. This appears to contradict the prediction from rate theory. Visualization of the microstructures, Figure 8(a-d), suggests, however, that the scale of decomposition may be dictated by the separation between sinks, rather than the system size. The precipitation morphology for the three alloy parameter sets is, in fact, influenced by the inverse Kirkendall effect, as detailed below.

The three alloys considered in the simulations are such that $D_B^i < D_A^i$, and therefore the permanent interstitial fluxes to the sinks favor solute depletion near the sinks in all three cases. In contrast, vacancy fluxes and the inverse Kirkendall effect favor solute segregation on sinks in parameter set 1, is neutral for parameter set 2, and favors solute depletion for parameter set 3. Overall, it is thus expected that solute precipitation should preferentially take place on the sinks for parameter set 1, and between sinks for parameter sets 2 and 3. This is indeed observed at 580 K, as seen in Figure 8. Note that owing to the formation of cherry-pit structures and to irradiation-induced kinetic

roughening of interfaces the *B*-rich precipitates develop non-equilibrium morphologies. At higher temperatures, 700 K and above, the precipitation morphology for parameter set 1 is different from the one observed at 580 K in the sense that precipitates are only found near the sinks. This transition from a finer to a coarser decomposition scale for parameter set 1, but not for parameter sets 2 and 3, is favored by the spherical geometry of the sink. The segregation of *B* atoms around the sinks for parameter set 1 is indeed concentrated on a smaller volume than the one for parameter sets 2 and 3, raising the local solute concentration to much higher values, thus promoting the growth of the precipitates that formed on the sinks, at the expense of the ones that formed away from the sinks. As mentioned in Section III.2.2, the exact nature of the phase separation for parameter set 1 at 700 K and above, see Figure 9, cannot be unambiguously determined with the simulation volumes employed in this study. Further work will be needed to determine whether the phase separation length scale is set by the sink separation distance, or by the system size.

Returning now to the compositional patterning regime, the three parameter sets produced distinct evolutions of the decomposition length scale. It is nearly independent of temperature for set 3, while it increases slightly for set 2 and significantly for set 1. These differences can be rationalized by considering the effect of alloying parameters on the forcing parameter γ. As the ballistic jump frequency was kept constant in the simulations, the characteristic phase separation length scale should be determined by the temperature dependence of D_B^{irr} (note that the number of forced relocations per displacement, *b*, has been adjusted so that all three parameter sets lead to a similar patterning length scale at low temperature; we also ignore the role of interstitials since

they have little influence on the diffusion of B atoms). The thermal solute diffusion

coefficient in alloys can be expressed as the product of the partial diffusion coefficient of

B atoms via vacancies and the vacancy concentration, i.e., $D_B = d_B^V C_V$. It is advantageous

to rewrite D_B as

$$D_B = \frac{d_B^V}{d_A^V} \cdot d_A^V C_V \qquad (7)$$

The matrix is highly diluted in B, and thus the defect regimes should be similar to those

found in pure A. Indeed, the vacancy diffusion coefficient can be written as

$D_V = d_V^A C_A + d_V^B C_B$, where d_V^A and d_V^B are the vacancy partial diffusion coefficient via

exchanging with A and B atoms, respectively. Note that, $d_A^V = d_V^A$ and $d_B^V = d_V^B$, since

either jump involves the exchange of a given atom-vacancy pair [14]. In the matrix where

C_B is small, we can thus approximate D_V as $D_V \approx d_V^A$. Therefore, in the sink elimination

regime, $d_A^V C_V^{irr} = D_A^{irr}$ should be approximately constant, and D_B^{irr} is mainly determined

by the ratio of two partial diffusion coefficients, $\dfrac{d_B^V}{d_A^V}$. This ratio was calculated as a

function of temperature in the dilute limit, using the standard five frequency model [35].

As shown in Figure 9(a) the partial diffusion coefficient ratio displays different

temperature dependencies for the three sets of parameters. For parameter set 1, the ratio

increases with temperature, resulting in a larger D_B^{irr}, and thus smaller γ and larger phase

separation length scale. This first effect dominates the evolution for parameter set 1. For

parameter sets 2 and 3, however, this analysis alone cannot fully explain the evolutions

reported in Figure 7. An additional effect that contributes to these evolutions is the fact

that point defects can be trapped at the chemical interfaces in a phase separated alloy,

lowering the concentration of "freely migrating" point defect [36]. This trapping effect

introduces another temperature dependence into C_V and thus D_B^{irr}. To incorporate this

effect, we measured in a set of separate KMC simulations the B diffusion coefficient in

an infinitely dilute A-B alloy with the same sink density and sink efficiency. Also, we

estimated the fraction of "freely migrating" point defects in the concentrated $A_{88}B_{12}$ alloy

by measuring the fraction of time that the vacancy has less than three B nearest neighbors.

This analysis suggests that the fraction of "freely migrating" vacancies have slightly

different temperature dependencies for parameter sets 1, 2, and 3 of, as shown in Figure

9(b). Finally, by combining the results from both effects, the relative partial diffusion

coefficients and the trapping of vacancies at chemical interfaces, we obtain a more

accurate estimation of D_B in the matrix of the concentrated alloy. Figure 9 (c) shows that,

for parameter set 1 and 2, D_B increases monotonically with temperature, while for

parameter set 3, D_B first increases, then reaches a plateau, and lastly drops slightly at the

highest temperatures. These temperature dependencies for D_B thus offer a clear

rationalization for the dependence of the compositional patterning length scale with

temperature reported in Figure 9 for the three alloy parameter sets.
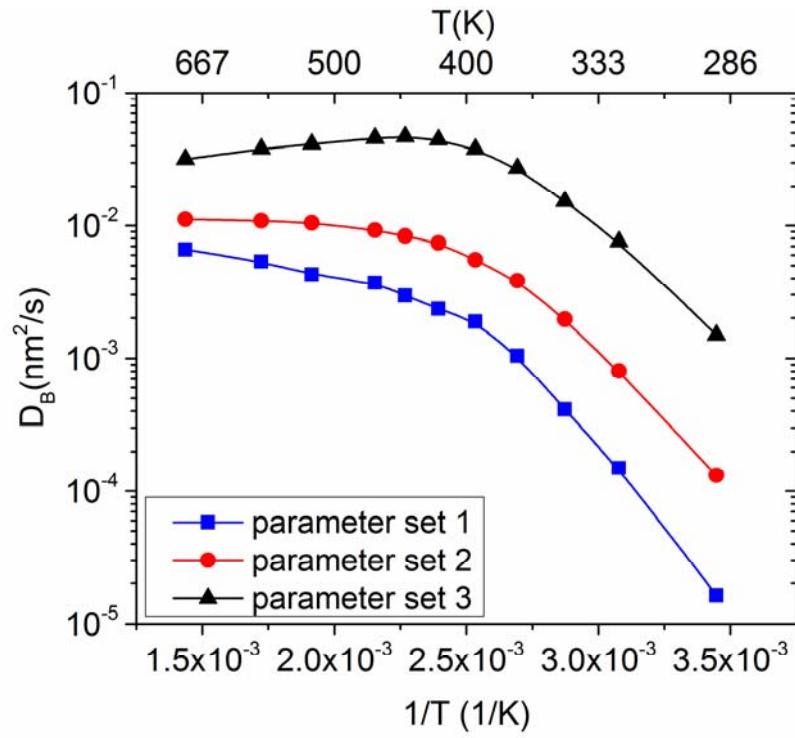
(a)
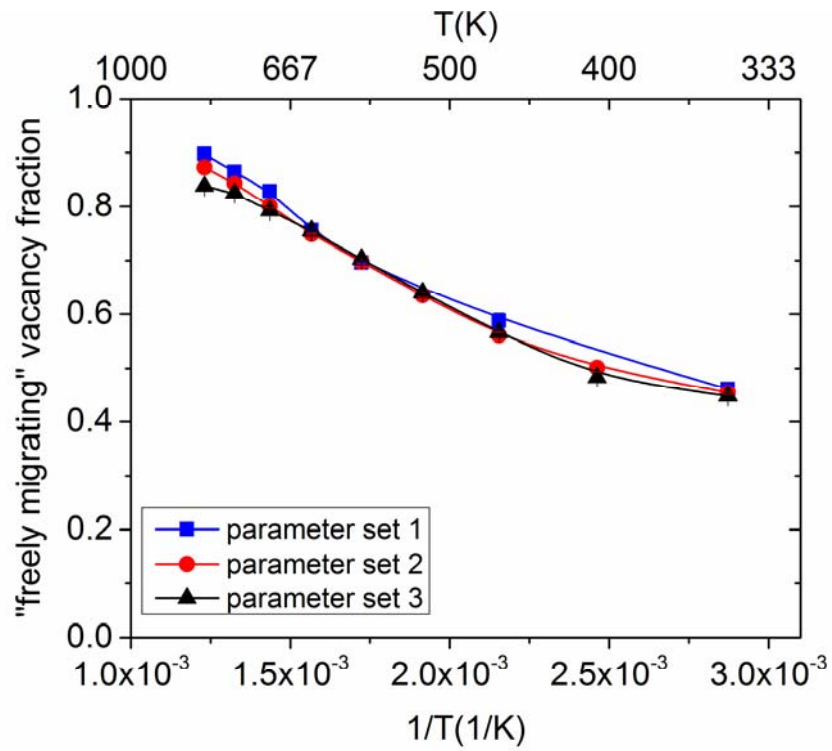
(b)
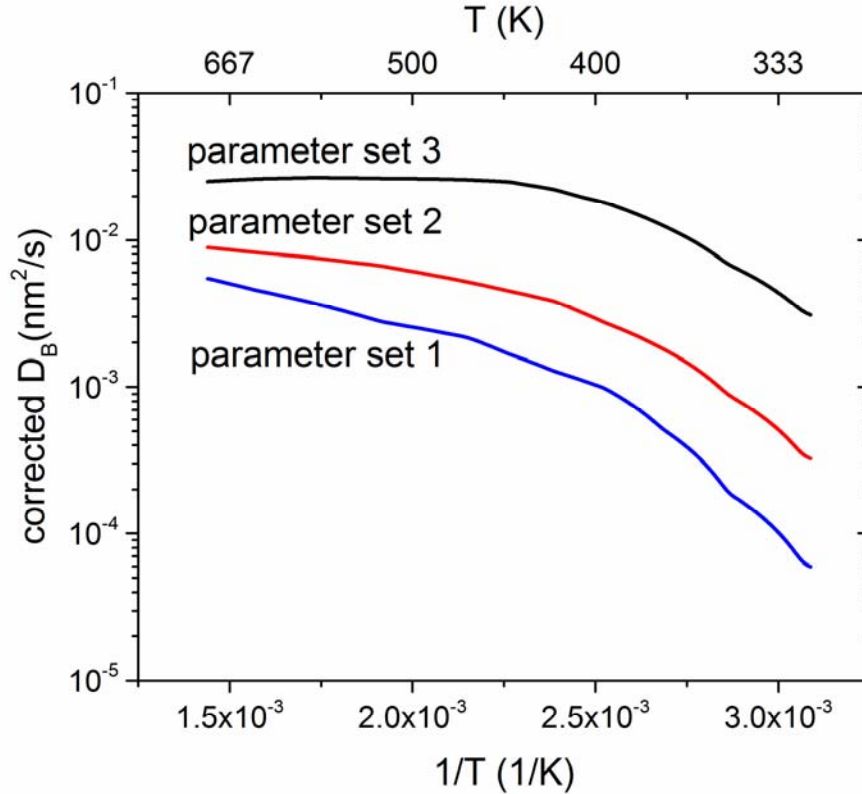
(c)

Figure 9   (a) *B* tracer diffusion coefficients for three sets of parameters, measured by KMC in a dilute limit (b) "freely migrating" vacancy fraction for three sets of parameters, measured by KMC in the $A_{88}B_{12}$ alloy (c) estimation of *B* diffusion coefficients for three sets of parameters in the $A_{88}B_{12}$ alloy after considering the "freely migrating" vacancy fraction (Color online)

The present KMC simulations relied on several, often used, simplifications [5,37], however they deserve some comment. The assumption of a rigid lattice makes it possible to reach steady state for fairly large simulated volumes, and while stress effects can influence point defect and atomic diffusion, it is expected that the key conclusions regarding the sink effects on compositional patterning would remain valid. Another simplification was ignoring the collective nature of atomic motion in displacement cascades [38]. Past modeling [5,7,18,34,39] and experimental works [4,18,19] indicate, however, that for modeling compositional patterning in moderately immiscible alloy systems such as Cu-Ag, Cu-Co or Cu-Fe the prevailing feature of cascades is the finite-

range of ballistic relocation distances. Following the detailed atomic modeling for $Cu_{50}Ag_{50}$ [6,39] this finite range mixing was modeled here as an exponential distribution with a decay length R. Another simplification of the present work is the neglect of defect clustering, either directly in displacement cascades or through the diffusion and reaction of point defects. These defect clusters should act as sinks and therefore they favor the stabilization of compositional patterning under irradiation. In addition, the sinks are modeled as geometrical sites and have no thermodynamic or strain interactions with solute atoms. In actual alloy systems, if present, these interactions could modify the sink efficiency of the nanoparticles and the stability of solute precipitates. This effect could be particularly important when solute precipitates form at the sinks, as observed for instance with parameter set 1, see Figure *8* (a,b). One more point is that the B-rich precipitates themselves, if semi-coherent or incoherent with the A-rich matrix, will provide sites for point defect elimination, promoting even further the stabilization of compositional patterning. One last point is that, we assume that the sink structure is stable for the whole range of irradiation temperatures investigated. In the case where nanoparticles serve as defect sinks, these nanoparticles could coarsen at high irradiation temperatures, and this would affect the sink strength. In particular, coarsening would result in a decreased nanoparticle number density and possibly a transition of the nanoparticle/matrix interfaces from semi-coherent to incoherent. The former effect would reduce the sink strength, while the latter could increase the sink efficiency of the interfaces. As a result, the characteristic length scale of the compositional patterns could change over large-dose irradiations. It will therefore be important to test experimentally the present simulation results and predictions. We note that progress in developing new nano-composite alloys,

offers a means to introduce a high density of stable small spherical sink particles in a matrix, either by severe plastic deformation and annealing, as in nano-ODS steels [9], or by intra-cascade precipitation during low temperature irradiation, as demonstrated in Cu-W and Cu-Mo alloys [4,40,41].

V.   Conclusion

In this work we investigate the effect of point defect regimes under irradiation on compositional patterning in model binary alloys. For that purpose, we extended existing KMC codes to allow for point defect production, recombination, and elimination on sinks, as well as irradiation-induced chemical mixing. The irradiation of pure metals is first used to validate and calibrate the KMC simulations using standard predictions from rate theory for the case of microstructures with planar and spherical sinks. This comparison provides a simple yet robust criterion, based on the fraction of point defects annihilated by recombination, to distinguish the steady-state point defect regimes of recombination and sink elimination. In the case of a model immiscible A-B alloy, the effect of point defect regimes on the temperature range of stability of irradiation-induced compositional patterning is then investigated using spherical sinks with various density and defect absorption efficiency. In the recombination regime, increasing irradiation temperatures leads to a continuous increase in steady-state B-rich precipitate sizes, and eventually to a transition to macroscopic phase separation, as expected from the Enrique-Bellon model. In the sink elimination regime, however, compositional patterning can be extended to much higher temperatures, in particular when the relative diffusivities of A and B atoms favor the depletion of B atoms at sinks via inverse Kirkendall effect. This stabilization of

the compositional patterning regime to high temperature is rationalized by the weak

temperature dependence of the forcing parameter in the sink-dominated regime.

Acknowledgement

Appendix A. Details of the KMC model and thermo-kinetic parameters

Irradiation induced Frenkel pairs are generated by first choosing two atoms, X and Y,

separated by a distance r_{xy}. A vacancy is then created on the lattice site initially occupied

by atom X, by moving X to form a dumbbell with Y. The distance r_{xy} could be chosen to

reproduce physical distributions, but here r_{xy} is chosen as a random distance within the

simulation cell, i.e., point defects are created uniformly in the cell. This choice is made so

that the production rates are equivalent to those used in rate theory modeling.

Recombination occurs when a vacancy and an interstitial come closer than a critical

distance, $d_{rec} = 3a_{nn}$, which corresponds to a recombination volume of 160 Ω (Ω is the

atomic volume), similar to values reported for Cu and other fcc metals [21]. During a

recombination event, one atom of the interstitial dumbbell is randomly chosen and moved

into the vacancy site, the other atom of the dumbbell remaining at the original dumbbell

site. In the case of the elimination of a vacancy on a sink site, an atom is assigned to the

site originally occupied by the vacancy. Following Soisson [23], we introduce a

'reservoir' of A and B atoms, which ensures the numerical stability of the program, and

the chemical composition of the overall system 'simulation cell + reservoir' is conserved.

When a dumbbell interstitial is absorbed at a sink site, one atom of the dumbbell is randomly chosen and moved to the reservoir. When a vacancy is absorbed at a sink site, an atom is randomly chosen from the reservoir to replace the vacancy. In practice, the reservoir size (0.1% of the total number of atoms in the simulation cell) is very small compared to the size of the simulation cell and it has no significant effect on the results.

As reviewed by Dederichs et al. [42] the dominant mechanism of dumbbell interstitial diffusion in fcc alloys is by isotropic diffusion of <100> dumbbells in three dimensions. We model these interstitial dumbbells by placing two atoms on one fcc lattice site and allowing either atom of the pair to jump to any of the 12 nearest neighbor sites. This corresponds to the case of a high rotation frequency of the interstitial dumbbells, for which the directionality of the dumbbells can be ignored [42]. With such approximation, during the exchange of an atom and a mixed dumbbell, two types of exchange occur with equal probabilities: $AB + A \rightarrow A + AB$ and $AB + A \rightarrow B + AA$.

The parameters of the kinetic model are related to physical quantities through the following relationships:

• homo-atomic pairwise interactions are related to cohesive energies for A and B metals through $E_{coh}^{A} = \dfrac{Z}{2}\varepsilon_{AA}$ and $E_{coh}^{B} = \dfrac{Z}{2}\varepsilon_{BB}$, where Z is the nearest-neighbor site coordination number ($Z = 12$ for fcc structure).

• hetero-atomic interactions are defined through the ordering energy, defined as $\omega_{AB} = 2\varepsilon_{AB} - \varepsilon_{AA} - \varepsilon_{BB}$, and a positive value of ω_{AB} results in an immiscible alloy at low enough temperatures, which will be the case in all alloys considered in this study.

• atom-defect effective interaction energies are used to reproduce realistic values of

defect formation energies, which are defined as $E_{for}^{XV} = Z\varepsilon_{XV} - \dfrac{Z}{2}\varepsilon_{XX}$ and

$E_{for}^{XI} = Z\varepsilon_{XI} - \dfrac{Z}{2}\varepsilon_{XX}$ (*X = A, B; I = AA, AB, BB*) for vacancies and various interstitials,

respectively, following the procedure introduced by Doyama and Koehler [43].

The thermo-kinetic parameters used in the KMC simulations are listed in Table 1.

The pre-exponential factor for all thermal jumps is set to be $10^{14}\,s^{-1}$. The *A*-V saddle

point energy was set so that the vacancy migration energy in the matrix is 0.8 eV, slightly

higher than its value in Cu [28]. Three distinct parameter sets are considered, see in Table

1, with different relative diffusivity of solute and solvent atoms, by varying the *B*-V

saddle point energy. For saddle point energies involving interstitials, the *A-AA* saddle

point energy is set to result in an interstitial migration energy of 0.37 eV, which is lower

than that of the vacancy, as found in Cu and other pure metals [44]. Although the

particular value of the interstitial migration energy we use in this study does not exactly

match the experimental value for Cu system, we note that since the intersitital migration

energy is still significantly lower than that of the vacancy, it has little effect on the main

results. Other saddle point energies involving interstitial jumps are set equal for

simplicity, but higher than that for the *A-AA* exchange. These settings capture the

diffusion characteristics of binary alloys with oversized solute atoms, i.e., where solute

atoms are mainly transported via vacancy mechanism.

Table 1 Thermo-kinetic parameters used in the KMC simulations. See text for definition of variables.

E_{coh}^A	E_{coh}^B	$E_{V,A}^{for}, E_{V,B}^{for}$	$E_{AA,A}^{for}, E_{AA,B}^{for}, E_{BB,B}^{for}$	$E_{AB,A}^{for}, E_{BB,A}^{for}, E_{AB,B}^{for}$
-4.34eV	-4.34eV	1.28eV	3.24eV	5.90eV

Parameter set	E_{AV}^{saddle}	E_{BV}^{saddle}	$E_{A,AA}^{saddle}$	$E_{X,I}^{saddle}$ (X,I combination other than A,AA)
1	-10.22eV	-9.83eV	-8.69eV	-8.26eV
2		-9.88eV		
3		-9.96eV		

Appendix B. Sink absorption probability and sink efficiency

For the case of planar sinks, we study here the relationship between the sink absorption probability p and the sink efficiency η, as defined by Eq. (6). Simulations were run at the same temperature and displacement rate used in Section III.1.1, but for system sizes of $200 \times 200 \times L_3$, with $L_3 = 12$ to 256. The resulting steady-state vacancy concentration is plotted as a function of the layer thickness, assuming different absorption probabilities, see Figure 10. For a perfect sink with absorption probability $p = 1$, the vacancy concentration varies as the square of the layer thickness when the thickness is small, as sink elimination dominates over recombination. For a poor sinks, i.e. with small p values, the vacancy concentration does not depend much on the layer thickness, as recombination always dominates.
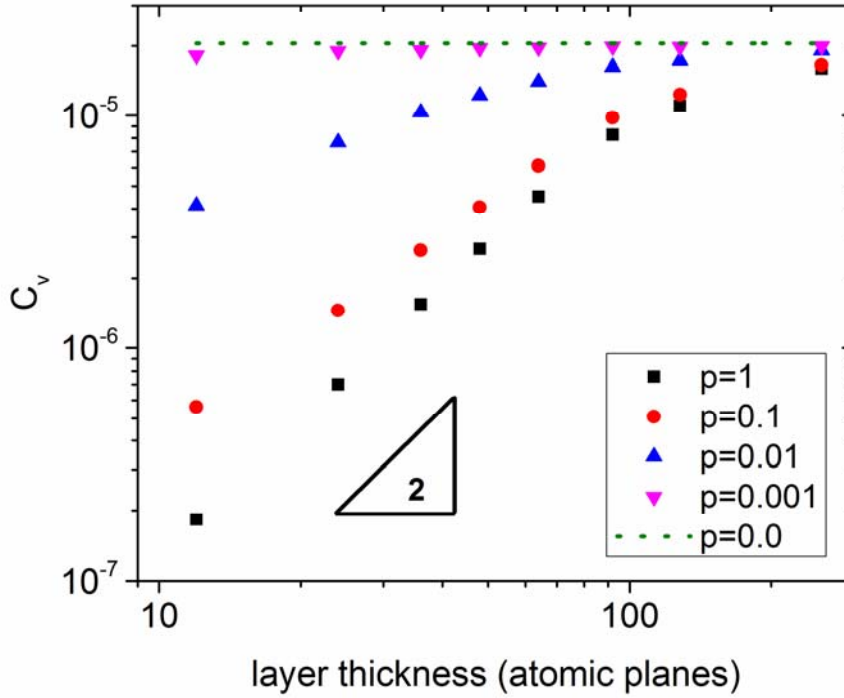
Figure 10 KMC simulation measured average vacancy concentration in the layer with constant absorption probability p. Irradiation temperature is *406 K*. (Color online)

For comparison, we also calculated using rate theory the vacancy concentration as a function of film thickness with constant sink efficiency η, see Figure 11. One notices that the shape of the constant p curves in Figure 10 and the constant η curves in Figure 11 are different. Although for perfect sinks, i.e., $p=1$ or $\eta=1$ or completely ineffective sinks, i.e., $p=0$ or $\eta=0$, the two descriptions are equivalent, for intermediate sink efficiencies, the two descriptions are very different. The description relying on the defect absorption probability p provides an intrinsic characteristic of that sink. On the contrary, the sink efficiency defined through Eq. (6) is affected by the distance between sinks, and the possible presence of other type of sinks.
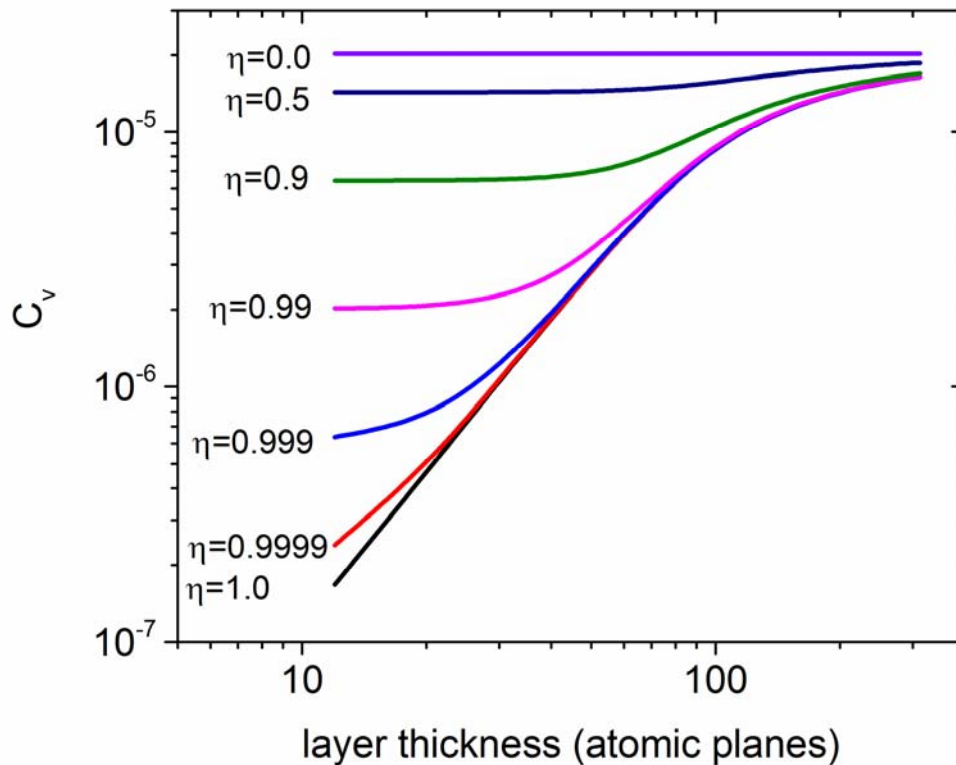
Figure 11 Rate theory calculated average vacancy concentration in the layer with constant sink efficiency η (Color online)

The difference between the two descriptions is more directly seen by plotting the sink efficiency η, measured during the KMC simulations, versus the sink absorption probability p, for various layer thicknesses, see Figure 12. The relationship between η and p can be highly non-linear. For p values below $\approx 1\%$, the η values obtained for different layer thickness deviate significantly from each other. For large thicknesses, near the center of the layer, recombination is the dominating mechanism for defect annihilation, and the values reflect fairly accurately the quality of the sink. For small layer thicknesses, however, the two boundaries of the layer can no longer be considered as isolated sinks, and point defect annihilation on one sink is affected by the presence of

nearby sinks (here the periodic image of the first sink). Therefore, the absorption

probability p is a more physical parameter for describing the quality of the sink. We note

also that the present description is equivalent to using a reaction rate that would

characterize the reaction and elimination of the point defects with the sink structure.
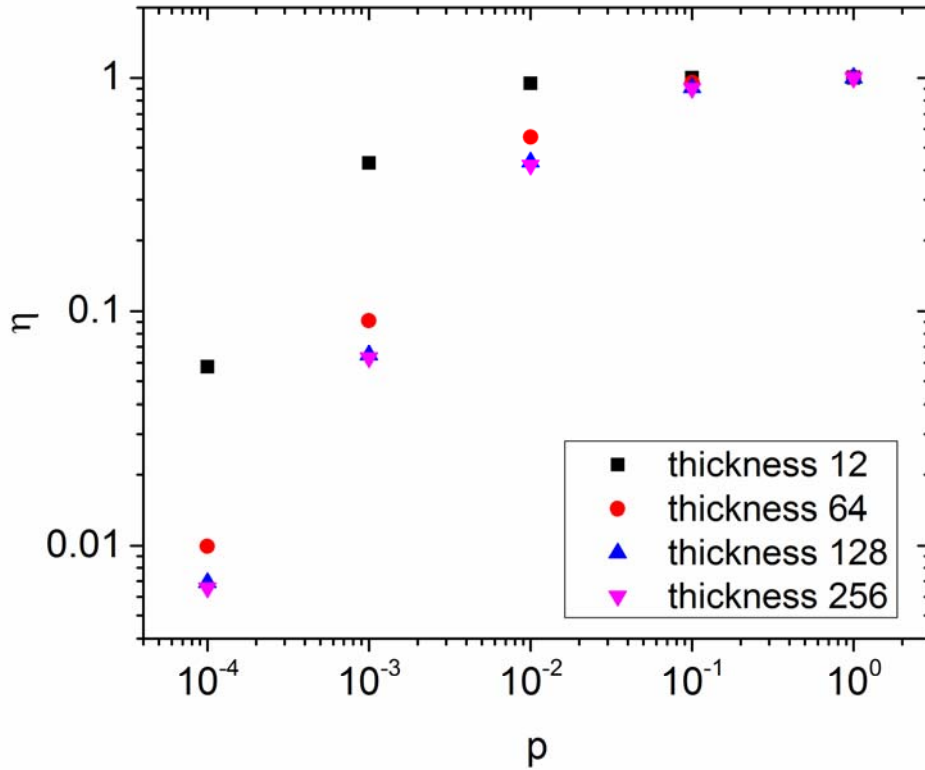
Figure 12 η as a function of p for different layer thickness (Color online)

Appendix C. Defect annihilation regimes for spherical sinks

We present here simulations evaluating the transition from recombination to sink

elimination for the case of spherical sinks, thus extending the results and analysis given

in Section III.1. Such sinks are for instance found in microstructures containing semi-

coherent or incoherent spherical precipitates. In order to test the effect of different sink

densities on sink efficiency, two sets of simulations were carried out with 1 or 8 spherical

sinks, uniformly embedded in a $64 \times 64 \times 64$ simulation cell, keeping the volume fraction

of sink sites fixed at ~0.1%, and the absorption probability at $p = 1.0$. The corresponding

sink densities, $3.2 \times 10^{23} m^{-3}$ and $2.6 \times 10^{24} m^{-3}$, are comparable to experimental

observations for some nano-ODS steels developed for nuclear applications [45,46]. The

transition temperature from recombination to sink elimination is lower for the higher sink

density, and, the diffusion coefficient in the sink regime is decreased by a factor 4, see

Figure 13. This is in agreement with rate theory, since, for a fixed fraction of sink sites,

the sink strength scales as $\left(N_p \right)^{2/3}$, N_p being the number of sink particles in the

simulation cell. Again, the recombination fractions at the transition point from

recombination to sink elimination, 29.9% and 27.9% for the low and high sink number

density respectively, agree well with the $\approx 30.9\%$ value predicted by rate theory.
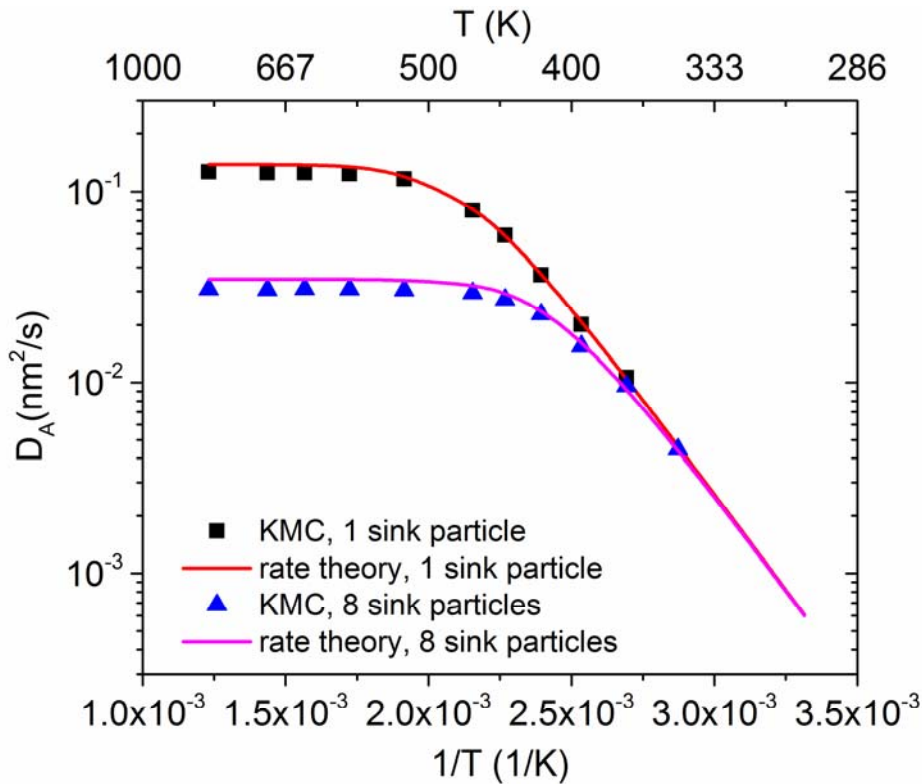
Figure 13 *A* atomic diffusion coefficients as a function of temperature for two sink densities, measured by KMC and calculated using rate theory (Color online)

References:

[1]   Cawthorne.C and E. J. Fulton, Nature **216**, 575 (1967).
[2]   N. M. Ghoniem, D. Walgraef, and S. J. Zinkle, J. Comput-Aided Mater. Des. **8**, 1 (2001).
[3]   R. S. Nelson, D. J. Mazey, and J. A. Hudson, J. Nucl. Mater. **44**, 318 (1972).
[4]   S. W. Chee, B. Stumphy, N. Q. Vo, R. S. Averback, and P. Bellon, Acta Mater. **58**, 4088 (2010).
[5]   R. A. Enrique and P. Bellon, Phys. Rev. B **63**, 134111 (2001).
[6]   R. A. Enrique, K. Nordlund, R. S. Averback, and P. Bellon, J. Appl. Phys. **93**, 2917 (2003).
[7]   R. A. Enrique and P. Bellon, Physical Review Letters **84**, 2885 (2000).
[8]   L. K. Mansur, Nucl. Technol. **40**, 5 (1978).
[9]   G. R. Odette, M. J. Alinger, and B. D. Wirth, in *Annual Review of Materials Research* (Annual Reviews, Palo Alto, 2008), pp. 471.
[10]   K. Tai, R. S. Averback, P. Bellon, Y. Ashkenazy, and B. Stumphy, J. Nucl. Mater. **422**, 8 (2012).
[11]   R. Cauvin and G. Martin, Phys. Rev. B **23**, 3322 (1981).
[12]   R. Cauvin and G. Martin, Phys. Rev. B **23**, 3333 (1981).
[13]   P. R. Okamoto and Wiedersich.H, J. Nucl. Mater. **53**, 336 (1974).

[14]   H. Wiedersich, P. R. Okamoto, and N. Q. Lam, J. Nucl. Mater. **83**, 98 (1979).

[15]   S. J. Zinkle and N. M. Ghoniem, Fusion Engineering and Design **51–52**, 55 (2000).

[16]   G. Martin, Phys. Rev. B **30**, 1424 (1984).

[17]   We note for completeness that the definition of γ in Eq. (1) involves here the chemical diffusion coefficient, allowing for a direct comparison with atomistic simulations, instead of the atomic mobility as in ref. [1]. This alternative choice does not alter the results since, in a mean-field approximation, mobility and chemical diffusion are directly related [5,16]

[18]   P. Krasnochtchekov, R. S. Averback, and P. Bellon, Phys. Rev. B **72**, 174102 (2005).

[19]   B. Stumphy, S. W. Chee, N. Q. Vo, R. S. Averback, P. Bellon, and M. Ghafari, J. Nucl. Mater. **453**, 66 (2014).

[20]   B. Stumphy, R. S. Averback, and P. Bellon, J. Mater. Res. **30**, 170 (2015).

[21]   R. Sizmann, J. Nucl. Mater. **69–70**, 386 (1978).

[22]   A. R. Allnatt and A. B. Lidiard, *Atomic Transport in Solids* (Cambridge University Press, Cambridge, 1993).

[23]   F. Soisson, J. Nucl. Mater. **349**, 235 (2006).

[24]   G. Martin and P. Bellon, in *Solid State Physics - Advances in Research and Applications, Vol 50*, edited by H. Ehrenreich, and F. Spaepen (Elsevier Academic Press Inc, San Diego, 1997), pp. 189.

[25]   D. B. Butrymowicz, J. R. Manning, and M. E. Read, Journal of Physical and Chemical Reference Data **2**, 643 (1973).

[26]   D. B. Butrymowicz, J. R. Manning, and M. E. Read, Journal of Physical and Chemical Reference Data **3**, 527 (1974).

[27]   D. B. Butrymowicz, J. R. Manning, and M. E. Read, Journal of Physical and Chemical Reference Data **5**, 103 (1976).

[28]   P. Ehrhart, *Atomic Defects and Diffusion Atomic Defects in Metals* (Springer, Berlin, 1991).

[29]   P. Bellon, S. J. Chey, J. E. Vannostrand, M. Ghaly, D. G. Cahill, and R. S. Averback, Surface Science **339**, 135 (1995).

[30]   J. Ye and P. Bellon, Phys. Rev. B **70**, 094104 (2004).

[31]   M. J. Demkowicz, R. G. Hoagland, B. P. Uberuaga, and A. Misra, Phys. Rev. B **84**, 104102 (2011).

[32]   A. P. Sutton and R. W. Balluffi, *Interfaces in crystalline materials* (Oxford University Press, Oxford, 1995), Monographs on the physics and chemistry of materials, 51.

[33]   R. S. Averback and M. A. Kirk, *Atomic Displacement Processes in Ion-Irradiated Materials* (American Society for Metals, Metals Park, 1987), Surface Alloying by Ion, Electron, and Laser Beams.

[34]   S. Shu, P. Bellon, and R. S. Averback, Phys. Rev. B **87**, 144102 (2013).

[35]   A. D. Le Claire, J. Nucl. Mater. **69–70**, 70 (1978).

[36]   M. Nastar and F. Soisson, Phys. Rev. B **86**, 220102 (2012).

[37]   C. S. Becquart and B. D. Wirth, *Kinetic Monte Carlo Simulations of Irradiation Effects* (Elsevier Science Bv, Amsterdam, 2012), Comprehensive Nuclear Materials, Vol 1: Basic Aspects of Radiation Effects in Solids/Basic Aspects of Multi-Scale Modeling.

[38]   R. S. Averback and T. D. de la Rubia, in *Solid State Physics*, edited by E. Henry, and S. Frans (Academic Press, 1997), pp. 281.

[39]   R. A. Enrique, K. Nordlund, R. S. Averback, and P. Bellon, Nuclear Instruments & Methods in Physics Research Section B-Beam Interactions with Materials and Atoms **202**, 206 (2003).

[40]   N. Q. Vo, S. W. Chee, D. Schwen, X. Zhang, P. Bellon, and R. S. Averback, Scr. Mater. **63**, 929 (2010).

[41]   X. Zhang, J. G. Wen, P. Bellon, and R. S. Averback, Acta Mater. **61**, 2004 (2013).

[42]   P. H. Dederichs, C. Lehmann, H. R. Schober, A. Scholz, and R. Zeller, J. Nucl. Mater. **69-7**, 176 (1978).

[43]   M. Doyama and J. S. Koehler, Acta Metallurgica **24**, 871 (1976).

[44]   P. Zhao and Y. Shimomura, Comput. Mater. Sci. **14**, 84 (1999).

[45]   M. Laurent-Brocq, F. Legendre, M. H. Mathon, A. Mascaro, S. Poissonnet, B. Radiguet, P. Pareige, M. Loyer, and O. Leseigneur, Acta Mater. **60**, 7150 (2012).

[46]   A. Certain, S. Kuchibhatla, V. Shutthanandan, D. T. Hoelzer, and T. R. Allen, J. Nucl. Mater. **434**, 311 (2013).